

# Complex impedance of a transition-edge sensor with sub- $\mu$ s time constant

Cite as: AIP Advances **10**, 035004 (2020); <https://doi.org/10.1063/1.5127100>

Submitted: 09 September 2019 • Accepted: 14 February 2020 • Published Online: 03 March 2020

 K. Hattori, R. Kobayashi, S. Takasu, et al.

## COLLECTIONS

Paper published as part of the special topic on [Photonics and Optics](#)



View Online



Export Citation



CrossMark

## ARTICLES YOU MAY BE INTERESTED IN

[Thermal fluctuation noise in Mo/Au superconducting transition-edge sensor microcalorimeters](#)

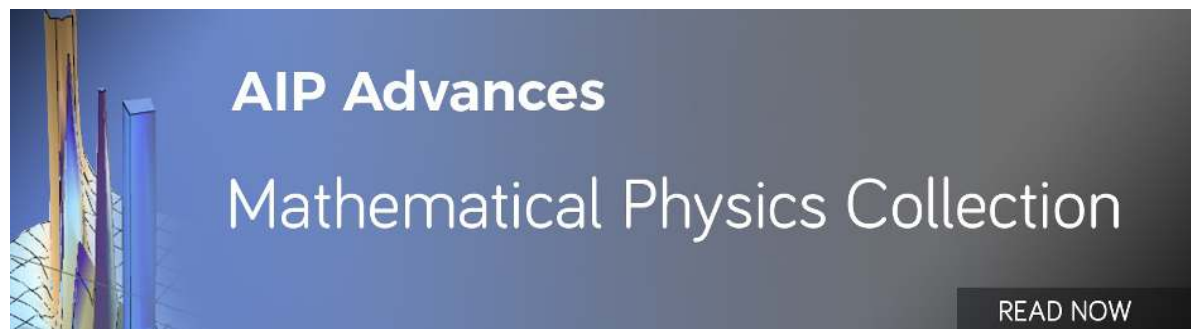
Journal of Applied Physics **125**, 164503 (2019); <https://doi.org/10.1063/1.5086045>

[Complex impedance, responsivity and noise of transition-edge sensors: Analytical solutions for two- and three-block thermal models](#)

AIP Advances **2**, 042110 (2012); <https://doi.org/10.1063/1.4759111>

[Impedance measurements and modeling of a transition-edge-sensor calorimeter](#)

Review of Scientific Instruments **75**, 1283 (2004); <https://doi.org/10.1063/1.1711144>



AIP Advances  
Mathematical Physics Collection

READ NOW

# Complex impedance of a transition-edge sensor with sub- $\mu$ s time constant

Cite as: AIP Advances 10, 035004 (2020); doi: 10.1063/1.5127100

Submitted: 9 September 2019 • Accepted: 14 February 2020 •

Published Online: 3 March 2020



K. Hattori,<sup>1,a)</sup>  R. Kobayashi,<sup>1,2</sup> S. Takasu,<sup>1</sup> and D. Fukuda<sup>1</sup> 

## AFFILIATIONS

<sup>1</sup>National Institute of Advanced Industrial Science and Technology, Tsukuba, Ibaraki 305-8563, Japan

<sup>2</sup>Institute of Quantum Science, Nihon University, Chiyoda-ku, Tokyo 101-8303, Japan

<sup>a)</sup> Author to whom correspondence should be addressed: [kaori.hattori@aist.go.jp](mailto:kaori.hattori@aist.go.jp)

## ABSTRACT

Optical transition edge sensor (TES) detectors that can resolve the energy of a single optical photon have proven to be desirable in multicolor fluorescence microscopy. Here, detectors with a higher energy resolution can distinguish dyes having similar or closer emission wavelengths, thus enabling the observation of multiple kinds of dyes simultaneously. To improve energy resolution, it is necessary to know how different the measured energy resolution is from the limit determined by the temperature sensitivity  $\alpha_1$  and current sensitivity  $\beta_1$ , as extracted from the complex impedance. Due to the very fast response of an optical TES (the time constant is shorter than 1  $\mu$ s), the complex impedance must be measured up to frequencies larger than 10 MHz. However, at high frequencies, the parasitic impedance in the circuit and reflections of electrical signals caused by discontinuities in the characteristic impedance of the readout circuits become significant. To reduce these effects, twisted pair cables are replaced with coaxial ones in this work; thus, a cleaner transfer function of the readout at high frequencies is obtained. The measured impedance of the studied TES is consistent with that given by the single-block model.

© 2020 Author(s). All article content, except where otherwise noted, is licensed under a Creative Commons Attribution (CC BY) license (<http://creativecommons.org/licenses/by/4.0/>). <https://doi.org/10.1063/1.5127100>

## I. INTRODUCTION

An ideal single-photon detector for quantum-information and biological-imaging applications should have a very high detection efficiency, photon-counting capability, and fast detector response characterized by small timing jitter and short recovery time. Recently, superconducting detectors such as transition-edge sensors (TESs)<sup>1</sup> and superconducting strip photon detectors (SSPDs, also called superconducting nanowire single photon detectors),<sup>2,3</sup> which are operated at cryogenic temperatures, showed remarkable features.

An optical TES consists of thin superconducting material and an optical cavity. TESs have exhibited a high detection efficiency of nearly 100% at near-infrared wavelengths,<sup>4,5</sup> a short time constant (0.2  $\mu$ s), and a very low dark-count rate, i.e., less than 1 Hz.<sup>6</sup> A TES is biased between normal and superconducting states. It is sensitive to change in temperature caused by the absorption of a photon. The pulse height of the output signal corresponding to absorption is associated with the change in temperature and photon energy. Therefore, a TES can resolve the energy of incident photons and

exhibit photon-number resolution. The energy resolution has been reported to be 0.1 eV at 0.8 eV (1550 nm)<sup>7</sup> and degraded slightly as the energy of incident photons increased.<sup>8</sup> An important feature of a TES is that it is sensitive to both near-infrared and visible photons over a wide energy range (from sub-eV to several eV).<sup>8</sup> In theory, a TES can detect photons as long as output signals are above the noise level. The detection efficiency can be enhanced by embedding a TES in an optical cavity, reaching nearly 100% at a target wavelength. Such a detector is also sensitive to photons at a wavelength other than the targeted one. Sensitivity in a wide range will open a new window in multicolor fluorescence microscopy and could enable the observation of fluorescence at visible and near-infrared wavelengths simultaneously.

SSPDs are intensively studied for applications in quantum information. An important property of SSPDs is a small jitter shorter than 100 ps.<sup>9,10</sup> A detection efficiency of 98% was achieved in the near-infrared region.<sup>11</sup> SSPDs do not exhibit intrinsic energy-resolving power. Recently, another type of detector with photon-counting capability, the optical microwave kinetic

inductance detector (MKID), was demonstrated.<sup>12</sup> Its energy resolution was 0.22 eV at 0.8 eV. The system detection efficiency of MKIDs has been improved but has not reached high efficiency.

Recently, biological imaging has emerged as a promising application of photon-counting detectors. A scanning microscope system with an optical TES has been proven to be a powerful tool for detecting faint light in the visible and near-infrared regions simultaneously.<sup>13</sup> The system also featured multicolor capability using cells labeled by two dyes.<sup>7</sup> Emission peaks of the applied dyes are typically within 500–800 nm,<sup>14</sup> and some are different by only tens of nanometers. Detectors with high energy resolution can distinguish such dyes and enable the observation of multiple dyes simultaneously. A detector with an energy resolution of the order of 10 nm could distinguish such dyes. The resolving power of the wavelength at  $\lambda$  can be associated with the energy resolution  $\Delta E$  and becomes

$$\Delta\lambda = \frac{\lambda^2}{hc} \Delta E. \quad (1)$$

The typical energy resolution of optical TESs at 550 nm (green) is 0.2 eV,<sup>8</sup> corresponding to  $\Delta\lambda = 50$  nm. Questions to be answered include whether the resolution of TESs can reach 10 nm and if the measured energy resolution will attain the theoretical limit. The theoretical energy resolution can be written by

$$\Delta E_{\text{FWHM}} = 2\sqrt{2 \ln 2} \sqrt{4k_B T^2 \frac{C}{\alpha_1} \sqrt{n(1+2\beta_1)}/2}, \quad (2)$$

where  $k_B$  is the Boltzmann constant,  $T$  is the temperature,  $C$  is the heat capacity,  $\alpha_1 = \frac{T}{R} \frac{\partial R}{\partial T} |_I$  is the temperature sensitivity,  $\beta_1 = \frac{I}{R} \frac{\partial R}{\partial I} |_T$  is the current sensitivity,  $R$  is the resistance of the TES,  $I$  is the current flowing through the TES, and  $n = 5$  is the electron-phonon limited conductance. To calculate energy resolution from Eq. (2), all the parameters should be measured.  $\alpha_1$ ,  $\beta_1$ , and  $C$  can be extracted from the complex impedance (response to small voltage signals). The complex impedance is the only probe of the current sensitivity  $\beta_1$ .  $\beta_1$  can be extracted from the high frequency limit of the complex impedance,  $Z(\omega \rightarrow \infty) = R_0(1 + \beta_1)$ , where  $Z$  is the complex impedance, and  $R_0$  is the resistance of the TES.<sup>1,15</sup> Therefore, accuracy in measurements carried out at high frequencies is important.

A challenge in exploring the parameters of optical TESs is that the detector response is fast and the impedance must be measured at up to a few tens of MHz, where parasitic inductance and stray capacitance in the readout become significant and reflections of electrical signals caused by discontinuities in the characteristic impedance of the readout circuits may affect the output signals. The difficulty in performing complex impedance measurements at high frequency prevented us from deriving  $\beta$ , which is calculated from the high frequency limit.<sup>16</sup>

In our previous work, we found that complex impedance measured above 0.1 MHz was inaccurate.<sup>17</sup> This was due to the difficulty in building a circuit model that takes parasitic impedance and reflections into account. When using an incorrect circuit model, the transfer function of the readout was erroneous, which led to errors in the complex impedance.

We presented an alternative method to estimate the transfer function without investigating the details of the entire circuit. We

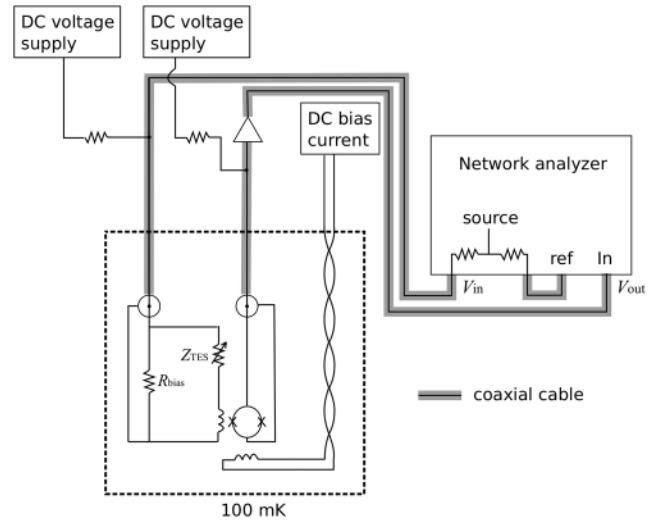


**FIG. 1.** Experimental setup: AC perturbations on the voltage bias and output superconducting quantum interference device (SQUID) signals are transferred through coaxial cables.

assumed the simplest thermal model consisting of a single heat capacity linked with the heat bath through conductance. The simple model seemed to describe our detector because the TES does not have an auxiliary absorber. Based on assumption of the model, we recalibrated the transfer function up to 30 MHz, successfully extracted the parameters, and compared them with values extracted from other kinds of measurements, finding them to be consistent.

However, the validity of the simple model should be examined with a reliable readout. In our previous work, we used twisted pair cables for signal transmission from the room temperature electronics to the cold readout and vice versa, through connectors and printed-circuit-boards (PC boards). Stray impedance was present, and there was discontinuity in characteristic impedance in the cables, connectors, and traces on the PC boards, thus making it difficult to construct a circuit model describing the readout. To make our readout more reliable, we replaced the twisted pairs with coaxial cables, as shown in Fig. 1. The new readout reduced both the stray impedance and points where the discontinuity in the characteristic impedance occurred. In this paper, we present measured complex impedance with the new readout and discuss a possible model to describe the complex impedance of an optical TES.

## II. COMPLEX IMPEDANCE MEASUREMENTS AT HIGH FREQUENCY

The complex impedance of a single-block TES, as shown in Fig. 2, can be written as

$$Z_{\text{TES}}(\omega) = R_0(1 + \beta_1) + \frac{R_0 \mathcal{L}}{1 - \mathcal{L}} \frac{2 + \beta_1}{1 + i\omega\tau_I}, \quad (3)$$

where  $G$  is the thermal conductance,  $\mathcal{L}$  is the constant-current loop gain given by  $\mathcal{L} = R_0 I^2 \alpha_1 / GT$ , and  $\tau_I$  is a time constant given by  $\tau_I = \tau_0 / (1 - \mathcal{L})$ , where  $\tau_0$  is an intrinsic time constant,  $C/G$ .<sup>1,15</sup> This

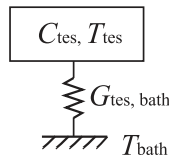


FIG. 2. The single-block model consisting of a TES and the heat bath.

TABLE I. Table of parameters associated with an optical TES and its readout.

| Material                                | Ti (20 nm)/Au (10 nm) |
|---|-----------------------|
| Size ( $\mu\text{m}^2$ )                | $5 \times 5$          |
| Critical temperature (K)                | $1.9 \times 10^{-1}$  |
| Normal resistance ( $\Omega$ )          | 3.2                   |
| Differential thermal conductance (pW/K) | $4.0 \times 10$       |
| Shunt resistance (m $\Omega$ )          | $1.8 \times 10$       |
| Series inductance (nH)                  | $1.8 \times 10$       |

is the simplest model and represents the TES directly coupled to the heat bath. The single-block model is thought to explain the behavior of an optical TES that does not possess any absorber. We will compare the measured complex impedance with that calculated by using Eq. (3) and discuss a possible thermal model later in this section.

We tested a bilayer TES consisting of 20 nm Ti and 10 nm Au layers. The size of the TES was  $5 \times 5 \mu\text{m}^2$ , and the TES was embedded in an optical cavity. The critical temperature  $T_c$  of the TES was 0.19 K, and the bath temperature was 0.1 K. The current flowing through the TES was converted to voltage by using a superconducting quantum interference device (SQUID), as shown in Fig. 1. The SQUID flux-locked loop (FLL) was kept open to measure the detector response at high frequencies. The flux bias was tuned to keep the bias point of the SQUID constant, when the voltage applied to the TES changed. Parameters associated with the TES and the readout are summarized in Table I. It should be noted that the series inductance shown in Table I is sum of the SQUID input and stray inductance. Its derivation will be described later in this section.

During complex impedance measurements, we injected small signals within the linear region of the SQUID. The small signals were generated by a network analyzer, as shown in Fig. 1, and perturbed the bias voltage applied to the TES. The incident signals were also sent to a reference port to be monitored. Signals from the SQUID were measured by the network analyzer and were calibrated by the reference signals. The input and output signals are transferred through coaxial cables, while DC flux bias was applied to the SQUID using a twisted pair cable. It should be noted that the calibration only corrected the responses of the network analyzer, and further corrections, to be described, were required.

An ideal bias circuit at 0.1 K can be converted to a Thévenin equivalent circuit consisting of an equivalent voltage source ( $V_{th}$ ) connected in series with the TES ( $Z_{TES}$ ), a resistor ( $R_s$ ), and an inductor ( $L$ ), as shown in Fig. 3(a).  $R_s$  is the sum of the bias and parasitic resistances in the circuit, and  $L$  is the stray inductance including the SQUID input.  $V_{th}$  is associated with signals from the signal generator at room temperature  $V_{in}$  by  $V_{th} = F(\omega)V_{in}$ , where  $F(\omega)$  is a transfer function. In an ideal circuit, the transfer function becomes  $F(\omega) = R_{bias}/(R + R_{bias})$ . In an actual setup, the function could be expressed by a more complicated formula.

The current flowing through the TES ( $I_{tes}$ ) is converted to voltage by the SQUID and amplified by room temperature electronics. The output signals  $V_{out}$  are associated with the current  $I$  by

$$V_{out} = G(\omega)I = \frac{G(\omega)F(\omega)V_{in}}{Z_{TES} + R_s + i\omega L}, \quad (4)$$

where  $G(\omega)$  is the transfer function modeling the output signal chain, including the SQUID and the amplifier at room temperature. In an ideal circuit,  $G(\omega)$  should stay constant regardless of  $Z_{TES}$ . Given that  $F(\omega)$ ,  $G(\omega)$ , and  $V_{th}$  are independent of  $Z_{TES}$ , one can take the ratio of signals in the normal state ( $V_n$ ) and the superconducting state ( $V_s$ ), and  $V_{th}$  and the transfer functions vanish.<sup>18</sup> Then,

$$\frac{V_s}{V_n} = \frac{R_n + R_s + i\omega L}{R_s + i\omega L}, \quad (5)$$

where  $R_n$  is the normal resistance. The value  $V_s/V_n$  is used to extract  $R_s$  and  $L$ . It is also useful to probe if  $G(\omega)$  and  $F(\omega)$  stay

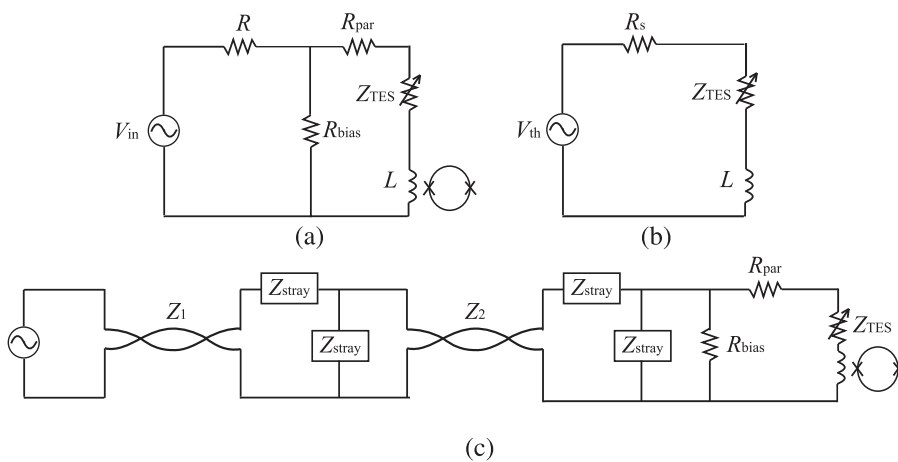


FIG. 3. Models of a TES bias circuit: (a) an ideal circuit, where the resistance  $R$  is much larger than  $R_{bias}$ , (b) the Thévenin equivalent circuit [applying the Thévenin theorem, (a) is equivalent to (b)], and (c) a possible circuit model of our previous readout using twisted pair cables, connectors, and PC boards;  $Z_1$  and  $Z_2$  are the characteristic impedances of the cables.  $Z_{stray}$  is the unwanted stray impedance present in the readout.

constant, and how well Fig. 3(b) represents the actual circuit. If the model is inappropriate,  $V_s/V_n$  could deviate from Eq. (5). The circuit model for the readout using twisted pairs and PC boards could be as shown in Fig. 3(c), which differs from the ideal circuit. Applying the Thévenin theorem to Fig. 3(c), the resultant equivalent circuit deviates from that shown in Fig. 3(b); thus,  $V_s/V_n$  diverges from Eq. (5). It should be noted that Fig. 3(c) has unknown stray impedance ( $Z_{stray}$ ) that prevents the correct equivalent circuit from being modeled. If coaxial cables are used, unwanted stray impedance is reduced, and the characteristic impedance becomes constant. Therefore, the equivalent circuit can be expressed well by Fig. 3(b).

Figure 4 shows the measured  $V_s/V_n$  in the new setup (coaxial cables) and the old readout (twisted pairs with PC boards and connectors). In the new readout, the deviation from Eq. (5) was improved, as shown in Fig. 4, whereas  $V_s/V_n$  in the previous setup deviated by more than 0.1 MHz. In Fig. 4(b), residuals to the fit

calculated from the absolute values were 7.6%. This implies that the new setup could be approximated well by the ideal circuit. The remaining residuals caused errors in  $R_s$ ,  $L$ ,  $F(\omega)$ , and  $G(\omega)$ . These errors propagated to  $Z_{TES}$ , which is calculated from  $Z_{TES}(\omega) = F(\omega)G(\omega)V_{in}/V_{out}(\omega) - R_s - i\omega L$ . The errors in  $V_s/V_n$  were considered in all analyses in this paper. It should be noted that the deviation at low frequencies, as shown in Fig. 4(a), was due to a bias tee. It was used to apply voltage-bias perturbed by small AC signals to the TES. It kept the characteristic impedance constant at high frequencies, but its properties became unideal at low frequencies. The higher noise level seen in Figs. 4(a) and 4(b) was due to transmission loss of the coaxial cables.

Figure 5 shows the measured complex impedance at  $R = 0.8$ , 0.6, and 0.3  $R_n$ , which fits to Eq. (3). The root mean squares (rmss) of the residuals to the fits shown in Fig. 5, calculated from the absolute values, are (a) 7.0%, (b) 7.0%, and (c) 7.5%, respectively. Note that the data above 15 MHz were excluded from the rms derivation.

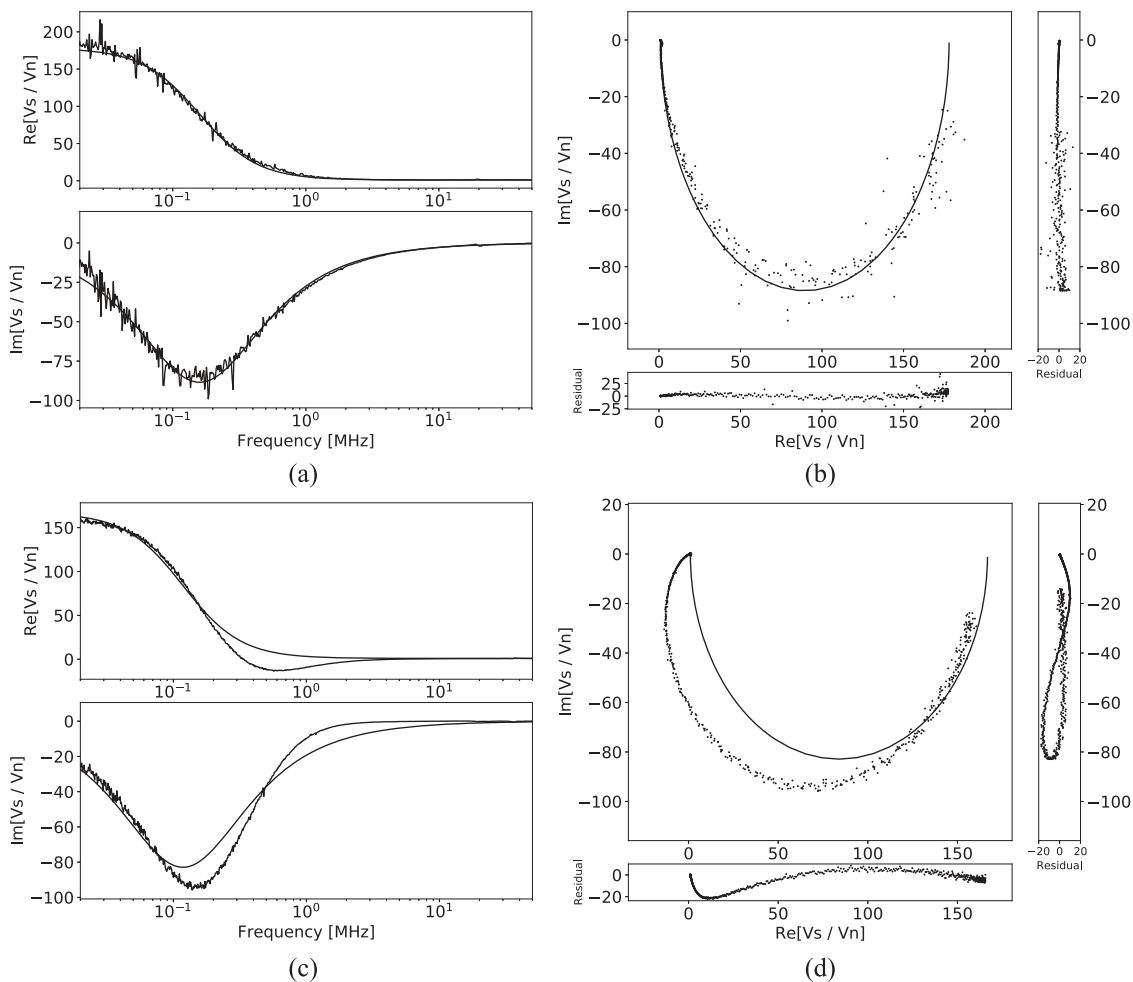


**FIG. 4.** Ratio of current flowing through the TES in the superconducting and the normal states, fitted to Eq. (5). Signals were transmitted and read out through coaxial cables [(a) and (b)] and twisted pairs [(c) and (d)]. Residuals to the fits are also shown. The root mean squares (rmss) of the residuals calculated from the absolute values are (b) 7.6% and (d) 37.0%.

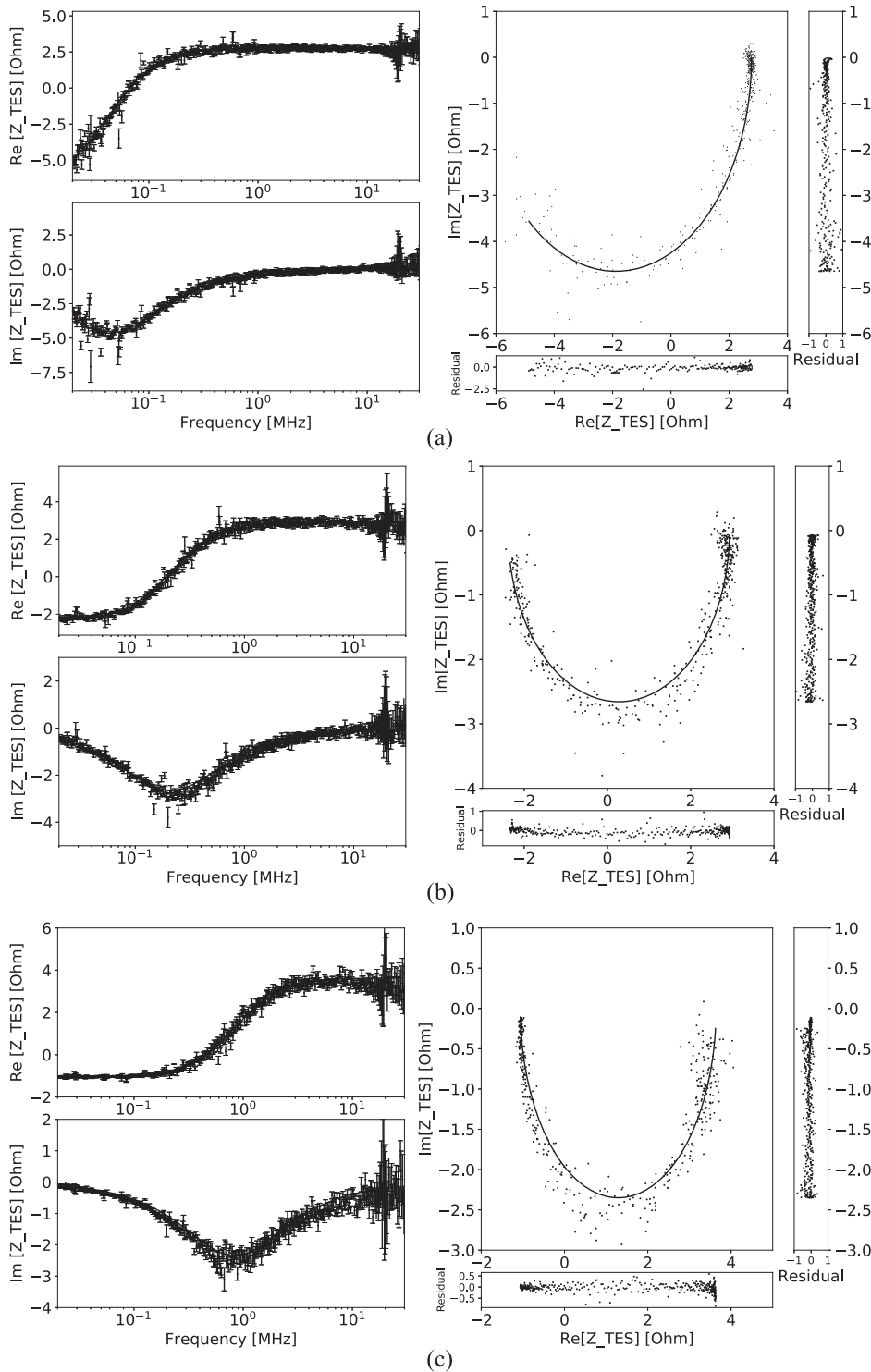


**FIG. 5.** Measured complex impedance and fit according to Eq. (3) (black lines). Coaxial cables were used for signal transmission. The TES was biased at points where the resistance was (a) 80%, (b) 60%, and (c) 30% of the normal resistance  $R_n$ . The loop gain in each panel was extracted from the measured complex impedance, and the rms of the residuals to the fits calculated from the absolute values (the resonant peak at around 15 MHz was excluded) are (a) 7.0%, (b) 7.0%, and (c) 7.5%.

The measured impedance was consistent with that given by the single-block model. Figures 6–8 show  $\alpha_I$ ,  $\beta_I$ , and the loop gain extracted from the measured complex impedance, respectively. Finally, the theoretical energy resolution limit calculated from

Eq. (2) and the measured complex impedance were 0.04 eV at 0.1  $R_n$ , while the measured resolution at the bias point was 0.15 eV. For photon detection, we used the old readout consisting of twisted pair cables and PC boards to have a SQUID flux-locked loop (FLL).



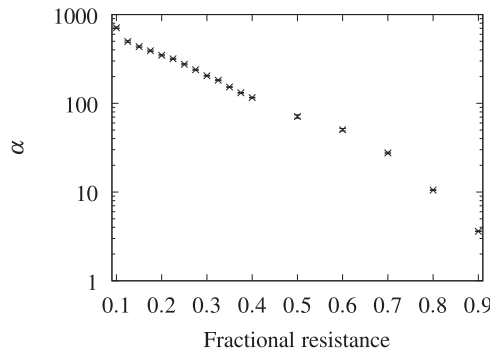


FIG. 6. The temperature sensitivity  $\alpha_1$ .

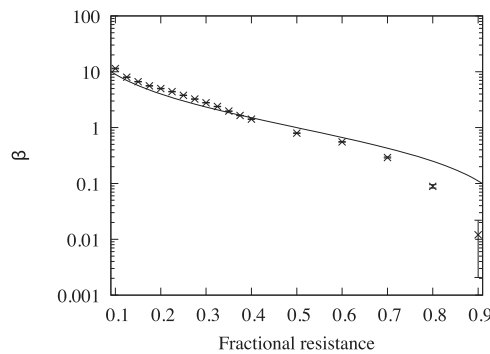


FIG. 7. The current sensitivity  $\beta_1$ . The upper limit with the two-fluid model is shown.

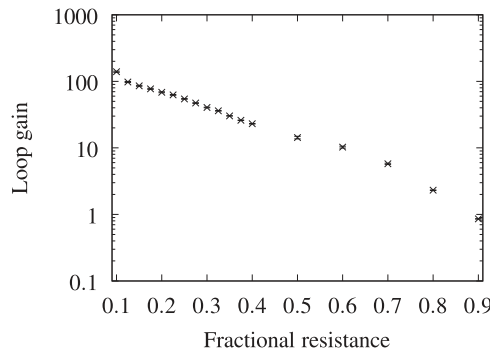


FIG. 8. Loop gain.

The TES was irradiated by a pulsed laser at 1550 nm (0.8 eV). The difference between the theoretical limit and the measured value could be due to escaping phonons<sup>19</sup> and excess noise.<sup>20</sup>

### III. DISCUSSION

In this section, we will explore another possible thermal model. The two-block model,<sup>21</sup> describing the behavior of a TES having

one additional block, was thought to be likely to present the thermal model of the optical TES. We chose the intermediate model, as shown in Fig. 9, which could describe the behavior of a TES without an absorber. The measured impedance was fitted to the complex impedance given by the model. The complex impedance of the intermediate model can be written as

$$Z_{TES}(\omega) = R_0(1 + \beta_1) + \frac{R_0 \mathcal{L}}{1 - \mathcal{L}}(2 + \beta_1) \times \left[ 1 + i\omega\tau_1 - \frac{G_{1,tes}(T_1)}{G_{1,tes}(T_1) + G_{1,bath}(T_1)(1 - \mathcal{L})} \frac{1}{1 + i\omega\tau_1} \right], \quad (6)$$

where  $T_1$  is the temperature in block 1,  $G_{1,tes}$  and  $G_{1,bath}$  are the differential thermal conductances between block 1 and the TES and between block 1 and the thermal bath, respectively.  $\mathcal{L}$  is the effective loop gain, given by  $\mathcal{L} = R_0 I^2 \alpha_1 / (G_{1,tes}(T_{tes})) T_{tes}$ , and  $\tau_1$  is a time constant given by  $\tau_1 = C_1 / (G_{1,tes}(T_1) + G_{1,bath}(T_1))$ , where  $C_1$  is the heat capacity of block 1. The measured impedance shown in Fig. 5 was fitted to Eq. (6), and the errors in the parameters associated with the additional block was huge, more than 100%.

To examine the possibility of the two-block model, we will also see the change in impedance curves made by the model. The time constant of the TES at a loop gain of zero was set to the typical value of the TESs studied here,  $\tau_0 = 7 \mu s$ . For simplicity, the thermal conductance was assumed to be  $G_{1,tes}(T_1) = G_{1,bath}(T_1)$ . The impedance was calculated for three cases; the time constant of the block 1 is (1) 100  $\mu s$ , (2) 10  $\mu s$ , and (3) 1  $\mu s$ , as shown in Figs. 10(a)–10(c), respectively. The calculated impedance deviated significantly at the low loop gain. It approached the impedance given by the single-block model as the loop gain became higher. The time constant of block 1 is also an important parameter. The effects of block 1 on the complex impedance reduced as the time constant  $\tau_1$  was faster. In Fig. 10(c), block 1 did not change the shape of the complex impedance. Eq. (6) and Fig. 10 suggest that the complex impedance is affected by thermal models at the low loop gain. The equation also shows that the deviation from the complex impedance given by the single-block model is expected to be of the order of  $1/\mathcal{L}$ . Therefore, to determine the thermal model, the complex impedance should be measured at the low loop gain.

As shown in Fig. 5(a), where the loop gain is small, the behavior of the optical TES agreed with that of the single-block model. The measured complex impedance at the low loop gain suggests

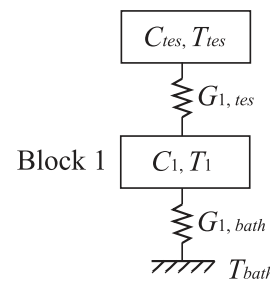
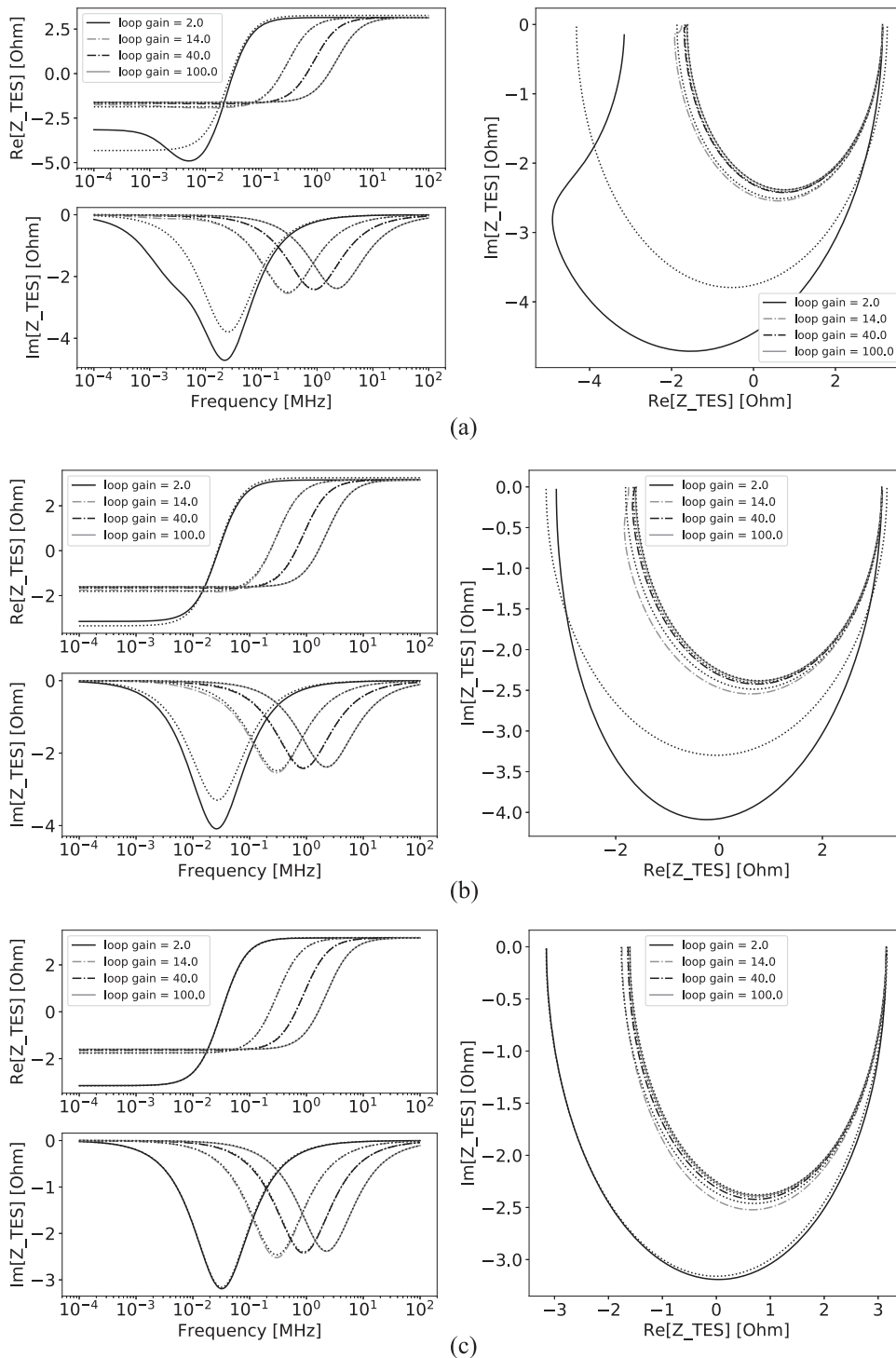


FIG. 9. The intermediate model consisting of a TES, a block, and the heat bath.



**FIG. 10.** Calculated complex impedance of the intermediate model with  $G_{1,tes}(T_1) = G_{1,bath}(T_1)$  and  $\tau_0 = \frac{C_{tes}}{\sum_{j=1}^{N+1} G_{tes,j}(T_0)} = 7 \mu\text{s}$ . The time constant of the intermediate block ( $\tau_1$ ) and the effective loop gain are varied, (a)  $\tau_1 = 100 \mu\text{s}$ , (b)  $10 \mu\text{s}$ , and (c)  $1 \mu\text{s}$ . The dotted lines show the best fit to the single-block model.

that the behavior of the optical TES should be described by the single heat capacity coupled to the heat bath. At  $0.3 R_n$  ( $\mathcal{L} = 40$ ), the deviation was expected to be of the order of  $1/\mathcal{L}$ , namely, by a few percent. The estimated deviation is consistent with that in the

measured impedance, considering the errors in the transfer function  $F(\omega)$ . From the complex impedance measurements, we conclude that the possibility of the intermediate model is low, and the single-block model is consistent with the measured complex



impedance. The frequency dependence of the intrinsic detector noise is also useful in exploring a possible thermal model. The thermal model is used to estimate the theoretical limit of energy resolution since thermodynamic fluctuations between the TES and the heat blocks (thermal fluctuation noise<sup>22,23</sup>) require knowledge of the thermal circuit.<sup>24</sup>

In Fig. 7, the highest values of  $\beta_1$  given by the two-fluid model ( $\beta_1 = R_n/R_0 - 1$ ) were overlaid. The measured  $\beta_1$  was below  $\beta_1 = R_n/R_0 - 1$  at large fractional resistances and exceeded it as the TES was biased deeper in the transition. The large  $\beta_1$  above the line could be explained by the resistively shunted junction (RSJ) model. Reduction of the Josephson effect might reduce  $\beta_1$  and enhance energy resolution. It should be noted that we did not confirm if the Josephson effect occurred in the optical TESs studied in this work. In future work, we will plan to carry out a well-established measurement to examine the Josephson effect; i.e., applying a magnetic field  $B$  to the TES and measuring its critical current  $I_c$  to see if  $I_c(B)$  presents the Fraunhofer pattern.

#### IV. CONCLUSION

We have shown that coaxial cables offered a cleaner readout transfer function for complex impedance measurements at high frequencies. By using the readout, we successfully tested a very fast TES detector with a time constant shorter than 1  $\mu$ s. The measured complex impedance was consistent with that given by the single-block model at both high and low loop gain. The theoretical energy resolution limit calculated from the measured complex impedance was 0.04 eV, while the measured resolution was 0.15 eV. In future work, to explore what made the gap between the theory and the measurements, excess noise and energy resolution degradation due to phonon escape will be examined.

#### ACKNOWLEDGMENTS

This work was supported by JSPS KAKENHI Grant No. JP17K14675. Transition-edge sensors were fabricated by the clean room for analog and digital superconductivity (CRAVITY) at the National Institute of Advanced Industrial Science and Technology (AIST). A part of this work was conducted at the AIST Nano-Processing Facility.

#### REFERENCES

- <sup>1</sup>K. D. Irwin and G. C. Hilton, "Transition-edge sensors," in *Cryogenic Particle Detection*, Topics in Applied Physics (Springer, 2005), pp. 63–152.
- <sup>2</sup>G. N. Goltsman, O. Okunev, G. Chulkova, A. Lipatov, A. Semenov, K. Smirnov, B. Voronov, A. Dzardanov, C. Williams, and R. Sobolewski, "Picosecond superconducting single-photon optical detector," *Appl. Phys. Lett.* **79**, 705–707 (2001).
- <sup>3</sup>C. M. Natarajan, M. G. Tanner, and R. H. Hadfield, "Superconducting nanowire single-photon detectors: Physics and applications," *Supercond. Sci. Technol.* **25**, 063001 (2012).
- <sup>4</sup>D. Fukuda, G. Fujii, T. Numata, K. Amemiya, A. Yoshizawa, H. Tsuchida, H. Fujino, H. Ishii, T. Itatani, S. Inoue, and T. Zama, "Titanium-based transition-edge photon number resolving detector with 98% detection efficiency with index-matched small-gap fiber coupling," *Opt. Express* **19**, 870–875 (2011).
- <sup>5</sup>A. E. Lita, A. J. Miller, and S. W. Nam, "Counting near-infrared single-photons with 95% efficiency," *Opt. Express* **16**, 3032–3040 (2008).

- <sup>6</sup>D. Fukuda, G. Fujii, T. Numata, A. Yoshizawa, H. Tsuchida, H. Fujino, T. I. H. Ishii, S. Inoue, and T. Zama, "Photon number resolving detection with high speed and high quantum efficiency," *Metrologia* **46**, 288–292 (2009).
- <sup>7</sup>D. Fukuda, K. Niwa, K. Hattori, S. Inoue, R. Kobayashi, and T. Numata, "Confocal microscopy imaging with an optical transition edge sensor," *J. Low Temp. Phys.* **193**, 1228–1235 (2018).
- <sup>8</sup>K. Hattori, S. Inoue, R. Kobayashi, K. Niwa, T. Numata, and D. Fukuda, "Optical transition-edge sensors: Dependence of system detection efficiency on wavelength," *IEEE Trans. Instrum. Meas.* **68**, 2253–2259 (2018).
- <sup>9</sup>I. E. Zadeha, J. W. N. Los, R. B. M. Gourgues, V. Steinmetz, G. Bulgarini, S. M. Dobrovolskiy, V. Zwiller, and S. N. Dorenbos, "Single-photon detectors combining high efficiency, high detection rates, and ultra-high timing resolution," *APL Photonics* **2**, 111301 (2017).
- <sup>10</sup>B. A. Korzh, Q.-Y. Zhao, S. Frasca, J. P. Allmaras, T. M. Autry, E. A. Bersin, M. Colangelo, G. M. Crouch, A. E. Dane, T. Gerrits, F. Marsili, G. Moody, E. Ramirez, J. D. Rezac, M. J. Stevens, E. E. Wollman, D. Zhu, P. D. Hale, K. L. Silverman, R. P. Mirin, S. W. Nam, M. D. Shaw, and K. K. Berggren, "Demonstrating sub-3 ps temporal resolution in a superconducting nanowire single-photon detector," [arXiv:1804.06839](https://arxiv.org/abs/1804.06839).
- <sup>11</sup>D. V. Reddy, A. E. Lita, S. W. Nam, R. P. Mirin, and V. B. Verma, "Achieving 98% system efficiency at 1550 nm in superconducting nanowire single-photon detectors," in *OSA Technical Digest (Optical Society of America, 2016)*, p. W2B.2.
- <sup>12</sup>W. Guo, X. Liu, Y. Wang, Q. Wei, L. F. Wei, J. Hubmayr, J. Fowler, J. Ullom, L. Vale, M. R. Vissers, and J. Gao, "Counting near infrared photons with microwave kinetic inductance detectors," *Appl. Phys. Lett.* **110**, 212601 (2017).
- <sup>13</sup>K. Niwa, T. Numata, K. Hattori, and D. Fukuda, "Few-photon color imaging using energy-dispersive superconducting transition-edge sensor spectrometry," *Sci. Rep.* **7**, 45660 (2017).
- <sup>14</sup>See <https://www.thermofisher.com> for Thermo fisher scientific, 2019.
- <sup>15</sup>M. Lindeman, S. Bandler, R. Brekosky, J. Chervenak, E. Figueroa-Feliciano, F. Finkbeiner, and C. K. M. Li, "Impedance measurements and modeling of a transition-edge-sensor calorimeter," *Rev. Sci. Instrum.* **75**, 1283–1289 (2004).
- <sup>16</sup>E. Taralli, L. Lolli, E. Monticone, M. Rajteri, L. Callegaro, T. Numata, and D. Fukuda, "Full characterization of optical transition-edge sensor by impedance spectroscopy measurements in a bandwidth extending to 1 MHz," in *ISEC 2013 IEEE 14th International Conference (IEEE, 2013)*.
- <sup>17</sup>K. Hattori, R. Kobayashi, T. Numata, S. Inoue, and D. Fukuda, "Complex impedance of fast optical transition edge sensors up to 30 MHz," *J. Low Temp. Phys.* **193**, 217–224 (2018).
- <sup>18</sup>K. Kinnunen, "Studies of transition-edge sensor physics: Thermal models and noise," Ph.D. thesis, The University of Jyväskylä, 2011.
- <sup>19</sup>A. G. Kozorezov, J. K. Wigmore, D. Martin, P. Verhoeve, and A. Peacock, "Resolution limitation in superconducting transition edge photon detectors due to downconversion phonon noise," *Appl. Phys. Lett.* **89**, 223510 (2006).
- <sup>20</sup>J. N. Ullom, J. A. Beall, W. B. Doriese, W. D. Duncan, L. Ferreira, G. C. Hilton, K. D. Irwin, C. D. Reintsem, and L. R. Vale, "Optimized transition-edge x-ray microcalorimeter with 2.4 eV energy resolution at 5.9 keV," *Appl. Phys. Lett.* **87**, 194103 (2005).
- <sup>21</sup>I. J. Maasilta, "Complex impedance, responsivity and noise of transition-edge sensors: Analytical solutions for two- and three-block thermal models," *AIP Adv.* **2**, 042110 (2012).
- <sup>22</sup>J. C. Mather, "Bolometer noise: Nonequilibrium theory," *Appl. Opt.* **6**, 1125–1129 (1982).
- <sup>23</sup>H. F. C. Hoevers, A. C. Bento, M. P. Bruijn, L. Gottardi, M. A. N. Korevaar, W. A. Mels, and P. A. J. de Korte, "Thermal fluctuation noise in a voltage biased superconducting transition edge thermometer," *Appl. Phys. Lett.* **77**, 4422 (2000).
- <sup>24</sup>N. A. Wakeham, J. S. Adams, S. R. Bandler, S. Beaumont, J. A. Chervenak, A. M. Datesman, M. E. Eckart, F. M. Finkbeiner, R. Hummatov, R. L. Kelley, C. A. Kilbourne, A. R. Miniussi, F. S. Porter, J. E. Sadleir, K. Sakai, S. J. Smith, and E. J. Wassell, "Thermal fluctuation noise in mo/au superconducting transition-edge sensor microcalorimeters," *J. Appl. Phys.* **125**, 164503 (2019).